

## Low-dose x-ray phase-contrast and absorption CT using equally sloped tomography

This content has been downloaded from IOPscience. Please scroll down to see the full text.

2010 Phys. Med. Biol. 55 5383

(<http://iopscience.iop.org/0031-9155/55/18/008>)

View [the table of contents for this issue](#), or go to the [journal homepage](#) for more

Download details:

IP Address: 195.220.108.81

This content was downloaded on 22/02/2017 at 12:06

Please note that [terms and conditions apply](#).

You may also be interested in:

[Analytical evaluation of the signal and noise propagation in x-ray differential PCT](#)

Rainer Raupach and Thomas G Flohr

[Rational approximations for tomographic reconstructions](#)

Matthew Reynolds, Gregory Beylkin and Lucas Monzón

[Towards breast tomography with synchrotron radiation at Elettra: first images](#)

R Longo, F Arfelli, R Bellazzini et al.

[Statistical image reconstruction from limited projection data with intensity priors](#)

Essam A Rashed and Hiroyuki Kudo

[Analyser-based x-ray imaging for biomedical research](#)

Pekka Suortti, Jani Keyriläinen and William Thomlinson

[An iterative reconstruction method of complex images using expectation maximization for radial parallel MRI](#)

Joonsung Choi, Dongchan Kim, Changhyun Oh et al.

[Task-based measures of image quality and their relation to radiation dose and patient risk](#)

Harrison H Barrett, Kyle J Myers, Christoph Hoeschen et al.

[Comparison of different numerical treatments for x-ray phase tomography of soft tissue from differential phase projections](#)

Daniele Pelliccia, Raquel Vaz, Imants Svalbe et al.

[4D micro-CT for cardiac and perfusion applications with view under sampling](#)

Cristian T Badea, Samuel M Johnston, Yi Qi et al.

## Low-dose x-ray phase-contrast and absorption CT using equally sloped tomography

Benjamin P Fahimian<sup>1,2</sup>, Yu Mao<sup>3</sup>, Peter Cloetens<sup>4</sup> and Jianwei Miao<sup>1</sup>

<sup>1</sup> Department of Physics and Astronomy, and the California NanoSystems Institute, University of California, Los Angeles, CA 90095, USA

<sup>2</sup> Department of Radiation Oncology, Stanford University, Stanford, CA 94305, USA

<sup>3</sup> Department of Mathematics, University of California, Los Angeles, CA 90095, USA

<sup>4</sup> European Synchrotron Radiation Facility, BP 220, 6 Rue Jules Horowitz, 38043 Grenoble Cedex, France

E-mail: [miao@physics.ucla.edu](mailto:miao@physics.ucla.edu) and [fahimian@stanford.edu](mailto:fahimian@stanford.edu)

Received 11 February 2010, in final form 27 July 2010

Published 24 August 2010

Online at [stacks.iop.org/PMB/55/5383](http://stacks.iop.org/PMB/55/5383)

### Abstract

Tomographic reconstruction from undersampled and noisy projections is often desirable in transmission CT modalities for purposes of low-dose tomography and fast acquisition imaging. However under such conditions, due to the violation of the Nyquist sampling criteria and the presence of noise, reconstructions with acceptable accuracy may not be possible. Recent experiments in transmission electron tomography and coherent diffraction microscopy have shown that the technique of equally sloped tomography (EST), an exact tomographic method utilizing an oversampling iterative Fourier-based reconstruction, provides more accurate image reconstructions when the number of projections is significantly undersampled relative to filtered back projection and algebraic iterative methods. Here we extend this technique by developing new reconstruction algorithms which allow for the incorporation of advanced mathematical regularization constraints, such as the nonlocal means total variational model, in a manner that is consistent with experimental projections. We then evaluate the resulting image quality of the developed algorithm through simulations and experiments at the European Synchrotron Radiation Facility on image quality phantoms using the x-ray absorption and phase contrast CT modalities. Both our simulation and experimental results have indicated that the method can reduce the number of projections by 60–75% in parallel beam modalities, while achieving comparable or better image quality than the conventional reconstructions. As large-scale and compact synchrotron radiation facilities are currently under rapid development worldwide, the implementation of low-dose x-ray absorption and phase-contrast CT can find broad applications in biology and medicine using these advanced x-ray sources.

## 1. Introduction

Tomographic implementation of emerging transmission imaging modalities, such as synchrotron x-ray absorption and phase contrast imaging, present important applications to biology and medicine (Cloetens *et al* 1999, Langer *et al* 2008, Momose *et al* 1996, Nugent *et al* 1996, Bech *et al* 2009, Weitkamp *et al* 2008, Connor *et al* 2009). For instance, synchrotron absorption imaging allows for tunable elemental mapping of specimens, while phase contrast imaging offers 100–1000 times increased sensitivities in the hard x-ray region relative to absorption imaging (Cloetens *et al* 1999). However, due to the time intensive line scanning of parallel projections and concerns about radiation damage to biomedical specimens, tomographic implementation of these techniques for applications beyond that of material science is problematic. For instance, in the common in-line holography implementation of phase contrast CT, multiple detections (often 3 or 4) at different sample to detector distances are required to recover the phase data for each projection (Langer *et al* 2008); this, coupled with the tomographic requirement of multiple projections from many directions, yields the acquisition time impractical for *in vivo* imaging. Moreover, as both modalities utilize the transmission of ionizing radiation, the tomographic requirement of multiple projections gives rise to significant concerns about the radiation dose in potential biomedical applications. Consequently, techniques for both fast acquisition and low-dose tomography are necessary.

One method to simultaneously achieve both the objectives of reduction of acquisition time and radiation is to under-sample the number of tomographic projections. However, under this condition, conventional reconstruction algorithms do not yield adequate results due to the violation of Nyquist sampling criteria. Mathematically, the tomographic reconstruction then represents an ill-posed problem due to the presence of missing information, i.e. missing projections, and inconsistencies generated from the presence of noise. In other fields, such as coherent diffraction microscopy where somewhat an analogous missing information problem is encountered due to missing phase data of the diffraction recordings, iterative oversampling Fourier methods have proven to be a powerful and efficient techniques for solving missing information under noisy conditions for non-crystalline and nano-crystal samples (Miao *et al* 1999, Pfeifer *et al* 2006, Abbey *et al* 2008, Raines *et al* 2010). Since the Fourier slice theorem provides a Fourier relation for tomographic imaging, such methods to aid the recovery of missing information in tomographic reconstruction can be exploited. In particular, previously an exact Fourier-based oversampling method for tomographic reconstruction, termed equally sloped tomography (EST), has been developed (Miao *et al* 2005). Both numerical simulations and experimental results from coherent x-ray diffraction and electron microscopy have shown that EST enables more accurate image reconstructions even when the number of projections is significantly under-sampled relative to filtered back projection (FBP) and algebraic iterative methods (Miao *et al* 2006, Lee *et al* 2008, Mao *et al* 2010, Jiang *et al* 2010).

The purpose of this work is twofold. First, to further extend the capability of EST in dealing with the problem of missing data under noisy conditions, we develop and test a new tomographic reconstruction structure that allows for the flexible incorporation of regularization schemes. Total variation-based optimization has garnered attention for edge preserving regularization (Rudin *et al* 1992) as well as in the realm of compressed sensing (Candès *et al* 2006). However, the use of pure total variation models for realistic images has been shown to produce artificial patches; this is due to the choice of the bounded-variation space and the corresponding total variation norm. More recently, the nonlocal means regularization model has been introduced which denoises a region by not just the analysis of local pixel values, but also by weighting in nonlocal pixels of similar properties throughout the entire image. The basic assumption behind this is that a natural image contains repeating structures instead

of repeating pixels. This method has been proved to be successful to remove artifacts while keeping the regular pattern and texture containing in the image and has been extended to include variational method using functionals with nonlocal regularization (Gilboa and Osher 2008), and proven superior to many other image regularization methods as it considers the large-scale structure of the image beside the local differences between pixels, which makes it capable of preserving important detailed features in an image while removing artifacts effectively (Buades *et al* 2005). Here, an iterative Fourier-based tomographic reconstruction algorithm is introduced which incorporates the advanced total variation implementation of the nonlocal means regularization, in a manner that is strictly consistent with experimentally measured projections (Buades *et al* 2005, 2006, Gilboa and Osher 2008). Second, we implement the method on the absorption and phase contrast x-ray CT modalities, and through a series of experiments and simulations quantify the resulting image quality. We then explore the feasibility of radiation dose and acquisition time reduction through reducing the number of projections by determining the factor by which the number of projections can be undersampled while still producing reconstructions of equivalent or better quality relative to conventional full-dose FBP reconstructions, as measured by such metrics as resolution, signal-to-noise ratio (SNR), and contrast-to-noise ratio (CNR).

## 2. Theory

### 2.1. Fourier formulation

The Fourier slice theorem, which equates the 1D Fourier transform of the projection data at a given angle to a slice of the 2D Fourier transform of the reconstructed image at the same angle, forms the foundation of tomographic reconstruction (Kak and Slaney 2001, Natterer 2001). Although the theorem provides an elegant conceptual method for the reconstruction of tomographic data, the theorem's direct computerized application has thus far been problematic due to the fact that interpolations must be implemented in Fourier space since equally angled acquisitions result in a polar distribution of points in Fourier space, while conventional FFT algorithms utilize a Cartesian point set (Kak and Slaney 2001, Natterer 2001). Since it is believed that no direct accurate and fast polar to Cartesian discrete Fourier transform can be constructed in a manner analogous to the continuum polar Fourier transform (Briggs and Henson 1995), a variety of interpolative methods have been proposed, the most sophisticated of such methods include the utilization of the non-uniform FFT (NUFFT) (De Francesco and Ferreira da Silva 2004, Delaney and Bresler 1996, Matej *et al* 2004, Zhang-O'Connor and Fessler 2006). However, all such methods must utilize some degree of Fourier space interpolation; for example, in NUFFT techniques, the degree of interpolations is prescribed by necessary accuracy parameter that in turn controls the complexity of interpolations (Ware 1998, Greengard and Lee 2004).

Recently, the existence of a direct exact fast Fourier transform algorithm and its inverse between a related pseudopolar grid and the Cartesian grid, called the pseudopolar fast Fourier transform (PPFFT), has been proven (Averbuch *et al* 2008a, 2008b). In contrast to other techniques, the PPFFT consists of 1D operations with a complexity of  $O(N^2 \log N)$  comparable to the standard Cartesian FFT, and requires no accuracy parameters or interpolations, resulting in machine accuracy. As shown in figure 1(a), for an  $N \times N$  Cartesian grid, the corresponding pseudopolar grid is defined by a set of  $2N$  lines, with each line consisting of  $2N$  grid points mapped out symmetrically on  $N$  concentric squares. The  $2N$  lines are subdivided into a basically horizontal (BH) group defined by  $y = sx$ , where  $|s| \leq 1$ , and a basically vertical (BV) group defined by  $x = sy$ , where  $|s| \leq 1$ ; the BV and BH groups are

symmetric under the interchange of  $x$  and  $y$ . The pseudopolar lines are termed ‘equally sloped’ since the slope,  $s$ , of each successive line as defined above changes by an equal slope increment of  $\Delta s = 2/N$  as opposed to the polar grid lines which change by equal-angled increments. The fact that, in contrast to the polar grid, the vertical and horizontal displacements in each group are uniform when the grid is transversed horizontally or vertically is one reason for the existence of a direct fast Fourier transform between the pseudopolar and Cartesian grids. More importantly, it has been shown that an exact and faithful notion of the Radon transform can uniquely be constructed along the lines of the pseudopolar grid. It is important to note that the history of such a grid dates back to 1974 to the work of Mersereau and Oppenheim (1974) who proposed a non-Cartesian ‘concentric square grid’ in Fourier space for image reconstruction. In the 1980s, such a grid was again utilized for tomographic reconstruction by Lawton (1988), Edholm and Herman (1987) and Edholm *et al* (1988). However it was not until the recent work of Averbuch *et al* (2008a, 2008b) that the mathematically faithful and algebraically exact PPFFT and its inverse was developed between the pseudopolar and Cartesian grids.

In contrast to the polar grid, the distance between sampling points along the lines of the pseudopolar grid varies from line to line. Subsequently, in order to map an equispaced object space input data onto a specific line on the pseudopolar grid, the fractional Fourier transform (FrFT) can be utilized to vary the output sampling distance of the Fourier transform. The 1D FrFT is equivalent to the standard discrete Fourier transform with the exception of a factor of  $\alpha$  (see equation (1)), controlling the output spacing, in the exponent (the FrFT reduces to the forward Fourier transform when  $\alpha = 1$  and to the inverse Fourier transform when  $\alpha = -1$ ) (Bailey and Swartztrauber 1991). Due to its similarity to FFT, the FrFT can be computed quickly using on the order of  $N \log(N)$  operations. By choosing an appropriate value for  $\alpha$ , the projection data can be mapped to the grid points of any line on the pseudopolar grid as shown in the next section. For the purpose of tomography, the FrFT of a projection can be related to the PPFFT of an object through an analog of the Fourier slice theorem which states that the 1D FrFT of a projection at an angle  $\theta$  is equivalent to a slice of the 2D PPFFT of the image at the same angle  $\theta$  in Fourier space.

## 2.2. Iterative reconstruction technique

While the PPFFT and its inverse provide an accurate method for the direct Fourier implementation of the Fourier slice theorem, experimentally an iterative algorithm is necessary to solve for the missing data and minimize the noise in order to properly address the limitations in the number of projections and source flux. In addition, as shown in figure 1(a), there exists a resolution circle in the pseudopolar grid because points beyond it cannot be obtained by applying the Fourier transform to the measured data (Miao *et al* 2005). Previously, an un-regularized iterative Fourier space algorithm, utilizing the pseudopolar transforms, was developed and experimentally implemented on the electron tomography modality (Miao *et al* 2005, Lee *et al* 2008); we build upon this method as follows.

As shown figure 1(b), the method developed here is structured to reach a compromise between the constraints and experimental projections by iterating back and forth between object and Fourier space, enforcing constraints in object space and strict conformity with experimental projections in Fourier space. The algorithm utilizes oversampling, i.e. sampling the Fourier domain more finely than the Nyquist frequency, similar to the methodology used to solve the phase problem in lens-less diffraction microscopy (Miao *et al* 1998, 1999). The effect of oversampling is to surround the object in real space by mathematical zeros, in a region called the support  $S$ , which the iterative algorithm can utilize as constraints. We note that the methodology can be experimentally implemented in two different ways. First, the projection

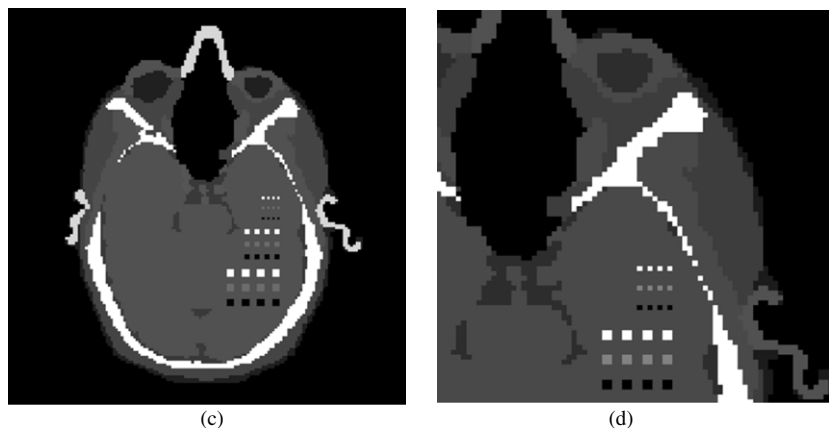


**Figure 1.** Methodology: (a) graphical relationship between the oversampled pseudopolar grid and the corresponding Cartesian grid, where  $N = 8$ . The black and white points delineate the BH and BV groups, respectively, and the dashed circle represents the resolution circle. (b) The  $j$ th iteration of the iterative algorithm as described in section 2.2; the dashed line indicates that the step occurs outside the loop in the initiating or terminating step. (c) Slice 82 of the Zubal head phantom with assigned linear attenuation coefficients (Zubal *et al* 1994). (d) Zoomed view of critical structures for comparisons with results of figure 3.

data can be acquired at angles corresponding to the equally sloped lines of the pseudopolar grid as first suggested in Miao *et al* (2005) and as experimentally implemented in Lee *et al* (2008); if so, the projections can be mapped onto the pseudopolar grid in Fourier space with machine accuracy using the FrFT, thereby eliminating all typical interpolations found in reconstruction algorithms. Second, as the PPFFT and inverse were first developed to provide an accurate substitute for the polar transform, conventional equally angled data can be mapped onto the pseudopolar grid accurately by rounding or interpolating to the nearest pseudopolar line. Furthermore, as inherently there exists a degree of inaccuracy in the alignment of projections at each angle experimentally, the said interpolation is justifiable. To emphasize this and the

generality of the method, the experimental reconstructions presented here utilize conventional equally angled acquisitions.

The algorithm is initiated by first padding the projections with zeros and calculating the oversampled Fourier slices using the FrFT in a manner such that the output spacing matches the spacing of the pseudopolar grid at the corresponding pseudopolar line; mathematically this is given by

$$F_\theta(k)|_{k \leq R} = \sum_{r=1}^L p_\theta(r) \exp(-2\pi i \alpha r k / 2N), \quad (1)$$

where  $F_\theta(k)|_{k \leq R}$  are the Fourier transform of the given projection  $p_\theta(r)$  within the resolution circle,  $\theta$  is the angle the projection makes with the  $x$ -axis,  $R$  is the radius of the resolution circle (as depicted in figure 1(a)),  $\alpha$  is equal to  $1/\cos(\theta)$  for BH lines and  $1/\sin(\theta)$  for BV lines, and  $L$  is an integer less than  $2N$ .

The  $j$ th iteration of the iterative algorithm can be broken down into the following steps.

- (i) Application of the inverse PPFFT to the Fourier space data  $F_\phi^j(\mathbf{k})$  to obtain an object space image  $f^j(\mathbf{r})$ ; if this is the initiating iteration, the Fourier data are the aggregation of the transformed experimental projections with the regions corresponding to the missing projections set to 0 or random numbers.
- (ii) Derivation of a new object through the regularization  $f^j(\mathbf{r})$  over a domain  $\Omega$ . For the reasons mentioned previously, in this paper we have chosen to present the first incorporation of the total variation implementation of the nonlocal means algorithm (NL) for regularized tomographic reconstruction (Buades *et al* 2006, Gilboa and Osher 2008). The particular NL algorithm used here is operated on  $f^j(\mathbf{r})$  to yield  $\bar{f}^j(\mathbf{r})$ ;  $\bar{f}^j(\mathbf{r})$  is defined as the solution of the following optimization problem and can be obtained by the steepest descent method or other recent advanced method:

$$\bar{f}^j(\mathbf{r}) = \arg \min_u J_w(u(\mathbf{r})) + \frac{\lambda}{2} \|u(\mathbf{r}) - f^j(\mathbf{r})\|^2, \quad (2)$$

where

$$J_w(u(\mathbf{r})) = \int_{\Omega} \sqrt{\int_{\Omega} (u(\mathbf{r}_1) - u(\mathbf{r}_2))^2 w_{u(\mathbf{r}),h}(\mathbf{r}_1, \mathbf{r}_2) d\mathbf{r}_2} d\mathbf{r}_1 \quad (3)$$

is the nonlocal total variation with respect to the weight function describing the similarity between the patches around different pixels. Given the reference image  $u(\mathbf{r})$ , which is generally taken as the noisy image prior to regularization, and a filter parameter  $h$ ,  $w_{u(\mathbf{r}),h}$  is a function on  $\Omega \times \Omega$ , defined as

$$w_{u(\mathbf{r}),h}(\mathbf{r}_1, \mathbf{r}_2) = \exp \left\{ -\frac{G * (\|u(\mathbf{r}_1 + \cdot) - u(\mathbf{r}_2 + \cdot)\|^2)(0)}{2h^2} \right\}, \quad (4)$$

where

$$G * (\|u(\mathbf{r}_1 + \cdot) - u(\mathbf{r}_2 + \cdot)\|^2)(0) = \int_{\Omega} G(\mathbf{t}) \|u(\mathbf{r}_1 + \mathbf{t}) - u(\mathbf{r}_2 + \mathbf{t})\|^2 d\mathbf{t} \quad (5)$$

and  $G$  is the Gaussian kernel.

- (iii) Application of a positivity constraint by setting

$$f'j(\mathbf{r}) = \begin{cases} \bar{f}^j(\mathbf{r}) & \text{if } \mathbf{r} \in S \quad \text{and} \quad \bar{f}^j(\mathbf{r}) \geq 0 \\ 0 & \text{if } \mathbf{r} \notin S \quad \text{or} \quad \bar{f}^j(\mathbf{r}) < 0, \end{cases} \quad (6)$$

where  $S$  represents the support region due to the oversampling that is expected to contain zeros.



- (iv) Calculation of the new Fourier space data  $F_{\varphi}^j(\mathbf{k})$  through the application of the PPFFT to  $f_j'(\mathbf{r})$ .
- (v) Updating the corresponding experimentally measured Fourier slices,  $F_{\theta}(\mathbf{k})|_{|\mathbf{k}| \leq R}$ , and retaining the Fourier slices outside the resolution circle,  $F_{\theta}^j(\mathbf{k})|_{|\mathbf{k}| > R}$  and the missing Fourier slices,  $F_{\phi}^j(\mathbf{k})$  by

$$F_{\varphi}^j(\mathbf{k}) = F_{\theta}(\mathbf{k})|_{|\mathbf{k}| \leq R} \cup F_{\theta}^j(\mathbf{k})|_{|\mathbf{k}| > R} \cup F_{\phi}^j(\mathbf{k}), \quad (7)$$

where  $\varphi = \theta \cup \phi$  is the complete set of angles for the pseudopolar grid,  $\theta$  is the set of angles of the measured projections and  $\phi$  is the set of angles of the missing projections. In contrast to the 3D algorithm presented in Miao *et al* (2005), this algorithm does not contain a FFT across 2D slices in step (iv) nor its inverse FFT in step (i); as a result, this 2D form allows the algorithm to be readily parallelized by sending each 2D slice to a different CPU for 3D reconstructions.

During each iteration, an error function defined by

$$\text{Error} = \frac{\sum_{\mathbf{k}, \theta} |F_{\theta}^j(\mathbf{k})|_{|\mathbf{k}| \leq R} - F_{\theta}(\mathbf{k})|_{|\mathbf{k}| \leq R}|}{\sum_{\mathbf{k}, \theta} |F_{\theta}^j(\mathbf{k})|_{|\mathbf{k}| \leq R} + F_{\theta}(\mathbf{k})|_{|\mathbf{k}| \leq R}|} \quad (8)$$

is calculated. The iterations are automatically terminated when the error does not fall by certain percentage from previous iterations. In all simulations performed here, the algorithm was stopped when the error did not decrease by more than 1% from the tenth previous iteration. The parameters for the regularization in all the reconstructions presented were  $h = 0.02$ ,  $\lambda = 10^{-5}$ ;  $\Omega \times \Omega$  represents the full domain of the image which was inputted for regularization. In order to be completely consistent with the experimental data, the output of the algorithm is always the image resulting from the inversion of the Fourier data once the data has been updated with the experimental Fourier slices; no constraints or processing is applied after this point. The computation time of each iteration is on the order of a single FBP reconstruction; with respect to this, recently we have developed a gradient descent version of the EST algorithm which reduces the computation time for each iteration by up to 70% (Mao *et al* 2010); this algorithm is beyond the scope of this paper, but will be explored in subsequent papers.

### 3. Methods

#### 3.1. Experimental and simulation methods

To quantify the performance of the algorithm and evaluate its utility for limited angle tomography, tomographic reconstructions were performed as a function of the number of projections using both simulated and experimental data in the x-ray absorption and phase contrast CT modalities. The interaction of x-rays for these modalities can be quantified by the complex refractive index:

$$n = 1 - \delta - i\beta, \quad (9)$$

where the projection data in phase-contrast imaging is given by the phase change after transmittance of x-rays of wavelength  $\lambda$  through a distance of  $s$ :

$$\Phi = \frac{2\pi}{\lambda} \int \delta(s) ds, \quad (10)$$



while the projection data for absorption imaging are given by

$$-\log\left(\frac{I}{I_0}\right) = \frac{4\pi}{\lambda} \int \beta(s) ds, \quad (11)$$

where  $I_0$  and  $I$  are the un-attenuated and attenuated intensities, respectively.

Simulations were used to model the possible application of tunable monochromatic compact synchrotron x-ray absorption CT for biomedical applications. For this purpose, a segmented anthropomorphic phantom based upon the scans of a human by Zubal *et al* (1994) was constructed at a resolution of 3.24 mm. A monochromatic source with energy of 50 keV was used, as this would be the approximate dosimetric optimal energy based on Kerma considerations for a biomedical sample containing bone (Lewis 2004); using mass attenuation coefficients and densities from the NIST and ICRU data sets, corresponding linear attenuation coefficients were assigned to the segmented tissues (ICRU 1989). To more rigorously quantify the image quality, three sets of resolution markers of varying contrast were added to the interior of the skull as shown in figure 1(c); these consisted of squares of  $1 \times 1$  pixel separated by 1 pixel, squares of  $2 \times 2$  pixels separated by 2 pixels, and squares of  $3 \times 3$  pixels separated by 3 pixels; since the resolution may have dependences on contrast, three sets of materials were used for each marker set, consisting of high-contrast bone, medium-low contrast tissue with linear attenuation coefficient 30% above the surrounding brain matter and air were assigned to the arrays (linear attenuation coefficients of  $81.4 \text{ m}^{-1}$ ,  $40.7 \text{ m}^{-1}$  and  $0.0 \text{ m}^{-1}$ , respectively). As with most synchrotron sources, the simulated source to detector geometry was parallel. The number of simulated detector elements at each angle was 256 for which tomographic projections of the phantoms were calculated using the Radon transform along a set of equally angled and equally sloped lines for the conventional and EST reconstructions, respectively. The projections at each detector element position were exponentiated and weighted by an un-attenuated flux,  $I_0$ , to give the noiseless intensity at the detector. Poisson noise, as approximated by a Gaussian distribution with a standard deviation  $\sqrt{I_0}$ , was added to the intensities; the intensities were then log-inverted to arrive at the noisy projections. Based on the signal-to-noise ratio of experimental projection data in current implementations of x-ray absorption CT at the European Synchrotron Radiation Facility (ESRF), the un-attenuated flux  $I_0$  was approximated to  $5.0 \times 10^5 \text{ m}^{-2}$  for the simulations.

Experimentally, an image quality phantom consisting of three material inserts, a high intensity filament and a micro beads resolution insert, was scanned at ESRF to acquire both x-ray absorption and phase contrast projections. Specifically, the body of the phantom consisted of a 7.5 mm polymethylmethacrylate (PMMA) cylinder, and the three material inserts consisted of de-mineralized water, 99.6% ethanol, a lipid; the 0.125 mm filament consisted of 99.99% pure aluminum; the beads in the resolution insert consisted of a mixture of 0.1 mm and 0.2 mm monosized polymers. The x-ray source was produced at the 150 m imaging beamline at the ID19 experimental station at ESRF. For the x-ray absorption experiment, the beam energy was 15 keV, the source to phantom distance was 32 mm, and the effective detector size after binning to 512 detector elements was  $29.8 \mu\text{m}$ . A very fast acquisition method was employed to acquire the absorption data for which 200-projections were acquired uniformly in 3.6 s (1.8 ms/projection) by rotating the phantom. For the phase contrast experiments, a beam energy of 24 keV was used, and the phase data were attained using the in-line holography acquisition method coupled by the mixed phase retrieval algorithm presented in Langer *et al* (2008); the phantom to detector distance for the in-line method were 0.012, 0.1, 0.3 and 0.99 m, for which 1200 radiographs uniformly about  $180^\circ$  were detected at each distance; the detector was a FReLon camera with an effective element size of  $30 \mu\text{m}$  after binning (Labiche *et al* 2007, Langer *et al* 2008).

For reference, all data were also reconstructed using FBP reconstructions, for which the projections were padded with zeros, and the un-cropped Ram–Lak (i.e. ramp filter) in conjunction with piecewise cubic Hermite interpolating polynomial (PCHIP) for the backprojection process was utilized (Fritsch and Carlson 1980); since it was shown that the previous EST algorithm resulted in higher resolution images than FBP (Miao *et al* 2005, Lee *et al* 2008), the un-cropped Ram–Lak filter was specifically selected in order to avoid degradation of resolution due the suppression of high frequency data which may result through the use of other filters (Comtat *et al* 1998, Kak and Slaney 2001, Natterer 2001). The equally sloped projection data of the simulations were reconstructed using the algorithm developed in section 2.2. As mentioned above, the pseudopolar transform also provides an accurate approximation to the polar Fourier transform, and consequently, conventional data sets acquired at equal angle intervals can also be utilized by the algorithm developed here. To demonstrate this, and as well as to isolate the effect of the developed algorithm from the problem of interpolation, experimentally the same equally angled projections were utilized for both the EST and FBP reconstructions; although this removes the interpolation accuracy advantage of equal slope projections, it serves to quantify the effect of the algorithm, which is the subject of this work. Subsequently, for the EST reconstructions, the polar projections were interpolated to the nearest pseudopolar line as detailed in section 2.2.

### 3.2. Methods for quantification of image quality

As no one metric can adequately quantify the image quality of a reconstruction, an aggregate of metrics are calculated in this paper as follows. For simulations, where the original phantom is known, correlation to the original can be used as one measure of the accuracy of the reconstructions. A rigorous method to measure the correlation of complex images is by comparing Fourier coefficients as a function of spatial frequency through the Fourier ring correlation (FRC) (van Heel and Schatz 2005, Frank 2006). The FRC is capable of quantifying the resolving power as it provides a generalization of the modulation transfer function (MTF) (Nickoloff 1988; Nickoloff and Riley 1985) for complex objects, and reduces to the MTF when the comparison and reconstructed image are an impulse and point spread function. The FRC across ‘rings’ in Fourier space is defined as

$$\text{FRC}_{\text{rec,phant}}(k, \Delta k) = \frac{|\sum_{\mathbf{k}} F_{\text{rec}}(\mathbf{k}) F_{\text{phant}}^*(\mathbf{k})|}{\sqrt{\sum_{\mathbf{k}} |F_{\text{rec}}(\mathbf{k})|^2 \sum_{\mathbf{k}} |F_{\text{rec}}(\mathbf{k})|^2}} \bigg|_{|\mathbf{k}| \in [k, k+\Delta k]}, \quad (12)$$

where  $k$  represents the radial parameter in the Fourier space,  $\Delta k$  represents the frequency interval size of the rings such that  $k \in [k, k + \Delta k)$ , and the subscripts rec and phant refer to the reconstructed image and the original phantom, respectively. A FRC value of 1 represents 100% correlation while a value of 0 represents 0% correlation; the spatial frequency defined by the 0.5 value of the FRC curve, representing 50% correlation between the reconstructed image and the original phantom, is commonly taken as a numerical value of the resolution.

In order to quantify the resolution, and its dependence on contrast, a series of resolution markers have been added to the interior of the anthropomorphic phantom. Experimentally, one insert of the PMMA phantom includes aggregates of small polymer beads, for which the separating space between the beads can be used to evaluate the resolution. To measure the noise response of the two different techniques, the SNR, defined by the mean intensity of a region divided by the standard deviation, was measured for each segmented tissue region of the Zubal phantom and regions of interest in the experimental data. Additionally, the contrast-to-noise ratio (Bushberg 2002, Gayou and Miften 2007), defined here as the absolute value of the means of two segment regions divided by the mean of the standard

deviations of the two regions, was used to quantify the contrast between tissues of interest and experimental material inserts.

## 4. Results

### 4.1. Simulations

Simulations on slice 82 of the modified Zubal anthropomorphic head phantom (figures 1(c) and (d)) were carried out to quantify the image quality of the method as a function of the number of projections and its performance relative to standard equally angled FBP. Poisson noise was added to the projections corresponding to a fluence of  $5.0 \times 10^5 \text{ m}^{-2}$ . As the head is located within the central  $160 \times 160$  pixel portion of the field of view (FOV), according to the Nyquist radial sampling criteria, the number of projections required to avoid streaking artifacts for a pixel phantom is approximately  $160\sqrt{2}(\pi/2) \sim 360$ -projections (Kak and Slaney 2001). Subsequently, a series of simulations were performed by starting at a maximum of 360-projections and then systematically reducing the number of projections. For the FBP reconstructions, all projections were calculated at equal-angle increments uniformly distributed across  $180^\circ$ , while for EST reconstructions, the projections were calculated along equally sloped lines of the pseudopolar grid distributed across  $180^\circ$  at constant slope increments. The results for reconstructions with the under-sampled number of projections of 60, 90-projections, as well as the Nyquist sampled 360-projections are shown in figure 2. In addition to the developed algorithm in this work, results of a non-regularized EST algorithm, which is a 2D analog of the original 3D algorithm of Miao *et al* (2005), are presented in the middle column of figure 2. The reconstructions via the method developed in this work are more specifically denoted as EST-NL, to distinguish from the previous non-regularized versions. For the EST-NL reconstructions, the algorithm was terminated automatically when the previously mentioned error condition was reached, resulting in 65, 45 and 19 iterations for the reconstructions of 60-, 90- and 360-projections respectively. For the non-regularized reconstructions, the algorithm was also terminated automatically using the same error condition, resulting in 51, 33 and 12 iterations for the reconstructions of 60-, 90- and 360-projections respectively. Figure 3 quantifies the resolution and quality of the reconstructed images via the FRC with the original phantom, while tables 1 and 2 quantify the image quality via measurements of the SNR and the CNR for tissues of interest.

For the same number of projections, the FRC curves for the EST-NL reconstructions are significantly higher than the corresponding FBP reconstructions among all spatial frequencies indicating higher resolution and correlation for the EST-NL reconstructions; the results indicate that the EST-NL reconstructions with a reduced number of projections of 90 have higher correlation with the original phantom across all spatial frequencies than the fully sampled FBP with 360-projections. The visual comparison with the original phantom in figures 1(c) and (d) with reconstructions in figure 2 indicate sharper boundaries and visual correlation for the EST-NL reconstructions. Alternative to the FRC, the resolution is visually quantified by resolution markers; it is noted that medium contrast resolution markers are not well delineated in the FBP reconstruction. The results in tables 1 and 2 demonstrate that, for the same flux, the EST-NL reconstructions result in an average SNR that is 3.2 to 3.7 greater than the corresponding FBP reconstructions, and in an average CNR that is 2.6 to 4.2 greater than the FBP reconstructions, for the same number of projections; also it is noted that for nearly all tissues, the EST-NL reconstruction with a reduced number of projections result in a higher SNR and CNR than the FBP reconstruction at the full Nyquist sampling. The SNR and CNR

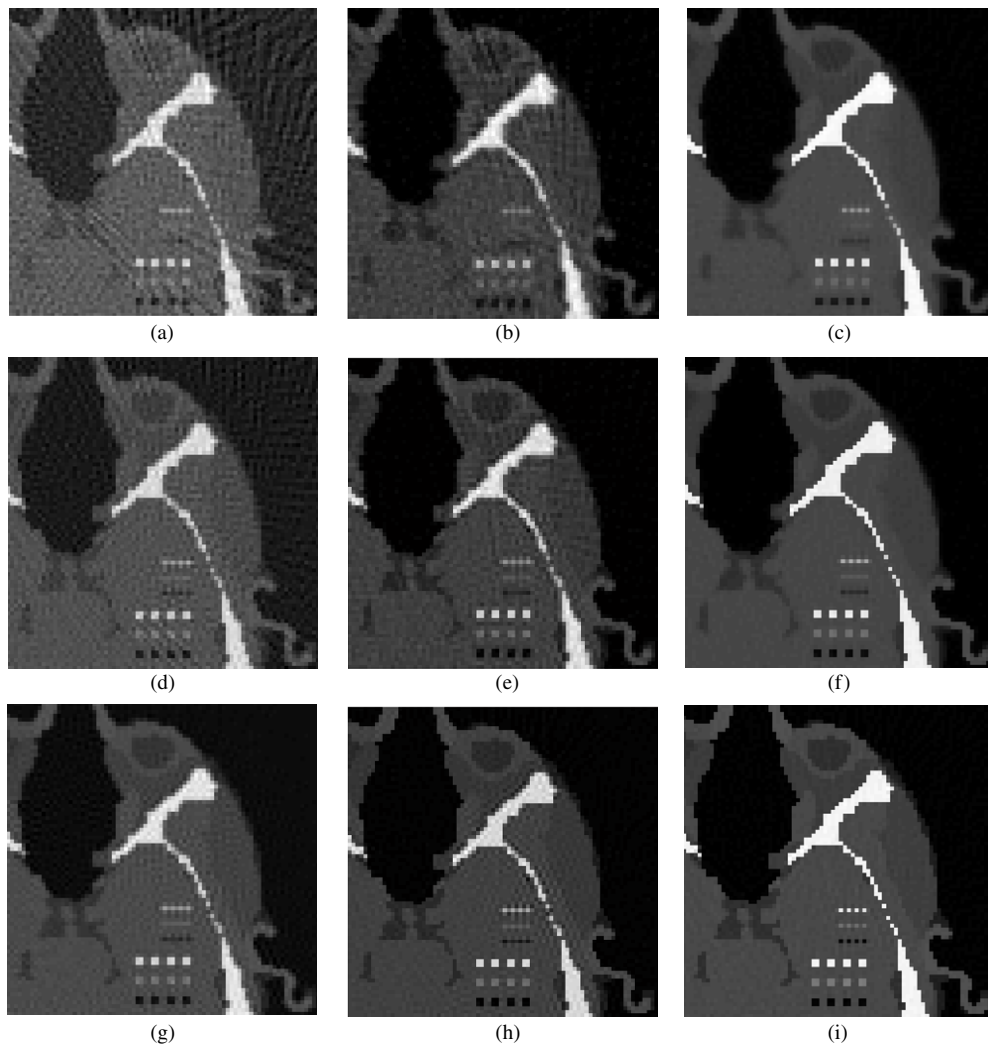


**Figure 2.** Simulation results. From left to right: the columns represent FBP reconstruction, reconstruction via the non-regularized method and the EST-NL developed here. From top to bottom: comparison of reconstructions using 60-, 90- and 360-projections, respectively. The displayed FOV is  $160 \times 160$  pixels.

results are visually confirmed in the greater recovery of low-contrast objects (such as in the mid-brain region), elimination of streaking artifacts and reduction of overall statistical noise.

#### 4.2. Experimental results

**4.2.1. X-ray absorption microtomography.** The experimental results for the x-ray absorption modality are displayed in figure 4; from left to right, in the first column are the various regions of interest for the full-dose FBP reconstruction with 200-projections, the 60% dose reduced FBP reconstruction with 80-projections and the 60% dose reduced EST-NL reconstruction with

**Table 1.** Comparison of the SNR for tissues of interest; flux =  $5 \times 10^5 \text{ m}^{-2}$ .

Projections	Method	Bone	Cartilage	Brain	Muscle	Fat	Cerebral fluid	Eye ext.	Eye int.	Skin	Mean of method/ FBP
60	FBP	8.5	3.9	4.3	3.6	3.1	2.4	3.7	2.6	1.6	1.0
60	Non-reg.	8.9	5.7	6.9	4.3	4.2	3.0	5.9	4.3	2.6	1.4
60	EST-NL	17.7	9.2	21.7	10.5	11.6	6.5	14.3	13.2	3.2	3.2
90	FBP	10.1	5.7	6.2	4.6	4.1	3.1	6.2	4.9	2.3	1.0
90	Non-reg.	10.7	7.5	8.4	5.0	5.0	3.7	8.3	7.0	3.5	1.3
90	EST-NL	29.9	15.5	27.5	16.6	14.7	8.8	18.1	14.6	4.0	3.2
360	FBP	11.2	8.8	9.8	5.6	5.5	3.7	12.8	11.0	4.1	1.0
360	Non-reg.	15.0	15.3	11.7	6.5	7.2	5.0	18.8	13.9	6.0	1.4
360	EST-NL	64.6	36.2	32.2	27.5	26.4	16.1	32.1	24.0	10.7	3.7

**Table 2.** Comparison of the CNR for tissues of interest; flux =  $5 \times 10^5 \text{ m}^{-2}$ .

Projections	Method	Brain to cerebral fluid	Muscle to fat	Bone to muscle	Bone to cartilage	Eye ext. to eye int.	Skin to fat	Skin to air	Mean of method/ FBP
60	FBP	1.1	0.6	6.8	6.9	1.3	1.7	1.6	1.0
60	Non-reg.	1.3	0.7	7.2	8.2	2.0	2.5	3.6	1.3
60	EST-NL	3.1	1.8	16.4	16.1	4.3	4.4	4.8	2.6
90	FBP	1.5	0.8	8.2	8.9	2.3	2.4	2.4	1.0
90	Non-reg.	1.9	0.9	8.9	10.1	3.1	3.1	5.1	1.2
90	EST-NL	4.8	2.5	27.5	26.4	5.7	5.5	6.1	3.0
360	FBP	2.0	1.0	9.4	11.0	4.8	3.7	5.9	1.0
360	Non-reg.	3.3	1.1	12.3	15.4	7.0	4.8	9.0	1.4
360	EST-NL	9.6	4.4	54.0	56.1	11.9	12.5	14.6	4.3

80-projections, respectively; from top to bottom are the whole phantom view, medium contrast region, low-contrast region and high-contrast resolution region. Visually, it is observed that the dose reduced FBP reconstruction in the second column is degraded by streaking artifacts and noise caused by the under-sampling of the projections while the dose reduced EST-NL reconstruction has recovered the missing data. To quantify reconstruction results, SNR and CNR were calculated for regions of interest; the SNR was defined as the mean pixel intensity of a region divided by the standard deviation of the intensities; the CNR between two regions of interest was defined as the absolute value of the difference of the mean of the first region and the second region divided by the mean of the standard deviations of the first region and the second region.

The results indicate that there is a significant deterioration in both SNR and CNR going from 200-projections to 80-projections for the FBP reconstructions; on average, both the SNR and CNR are approximately 50% lower for the FBP reconstruction with 80-projections than the FBP projection with 200-projections. On the other hand, the dose reduced EST-NL

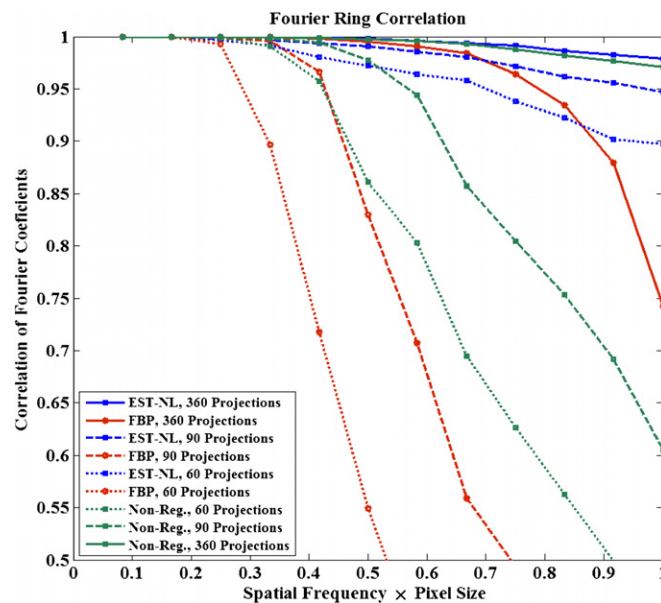


**Figure 3.** Fourier ring correlation of the reconstructed images to the original phantom for results presented in figure 2. The horizontal axis represents the spatial frequency normalized to the pixel size, which was 3.24 mm in the simulations.

(This figure is in colour only in the electronic version)

reconstruction with 80-projections outperforms not only the dose reduced FBP reconstruction, but also the full-dose FBP reconstruction among all measured metrics of SNR and CNR. On average, relative to the FBP reconstruction with the same number of projections, the SNR for the EST-NL reconstruction was 3.5 times greater, and the CNR is 3.4 times greater; relative to the full-dose FBP reconstruction, the SNR for the 60% dose reduced EST-NL reconstruction is 1.8 times greater, and the CNR is 1.7 times greater. Visual comparison of the beads, and the visibility of small void regions in between them, suggests that the EST-NL reconstruction has equal or better resolution than both FBP reconstructions.

**4.2.2. X-ray phase contrast CT.** Experimental results for the x-ray phase contrast CT modality are shown in figure 5. As with x-ray absorption experiments, the same equally angled data were utilized for the FBP and EST-NL reconstructions. The first column represents FBP with 200-projections which is below the Nyquist requirement, but represents an image quality that is acceptable for conventional reconstructions. The second and third columns represent the FBP and EST-NL reconstructions with 60-projections, respectively. From top to bottom is the comparison of the full field of view, contrast insert, resolution insert and zoomed area of the resolution insert. In general, it is noted that streaking artifacts degrade the under-sampled FBP reconstruction while the EST-NL reconstructions are void of such artifacts. To quantify the image quality, the SNR and CNR of the material insert shown was calculated relative to the PMMA background. The SNR was measured to be 32.1, 10.6 and 71.6 for the 200-projection FBP, 60-projection FBP and 60-projection EST-NL reconstruction, respectively. The CNR was measured to be 9.7, 3.4 and 19.9 for the 200-projection FBP, 60-projection FBP and 60-projection EST-NL reconstruction, respectively. The results are consistent with the visual appearance of the second row which suggests that the 60-projection EST-NL reconstruction



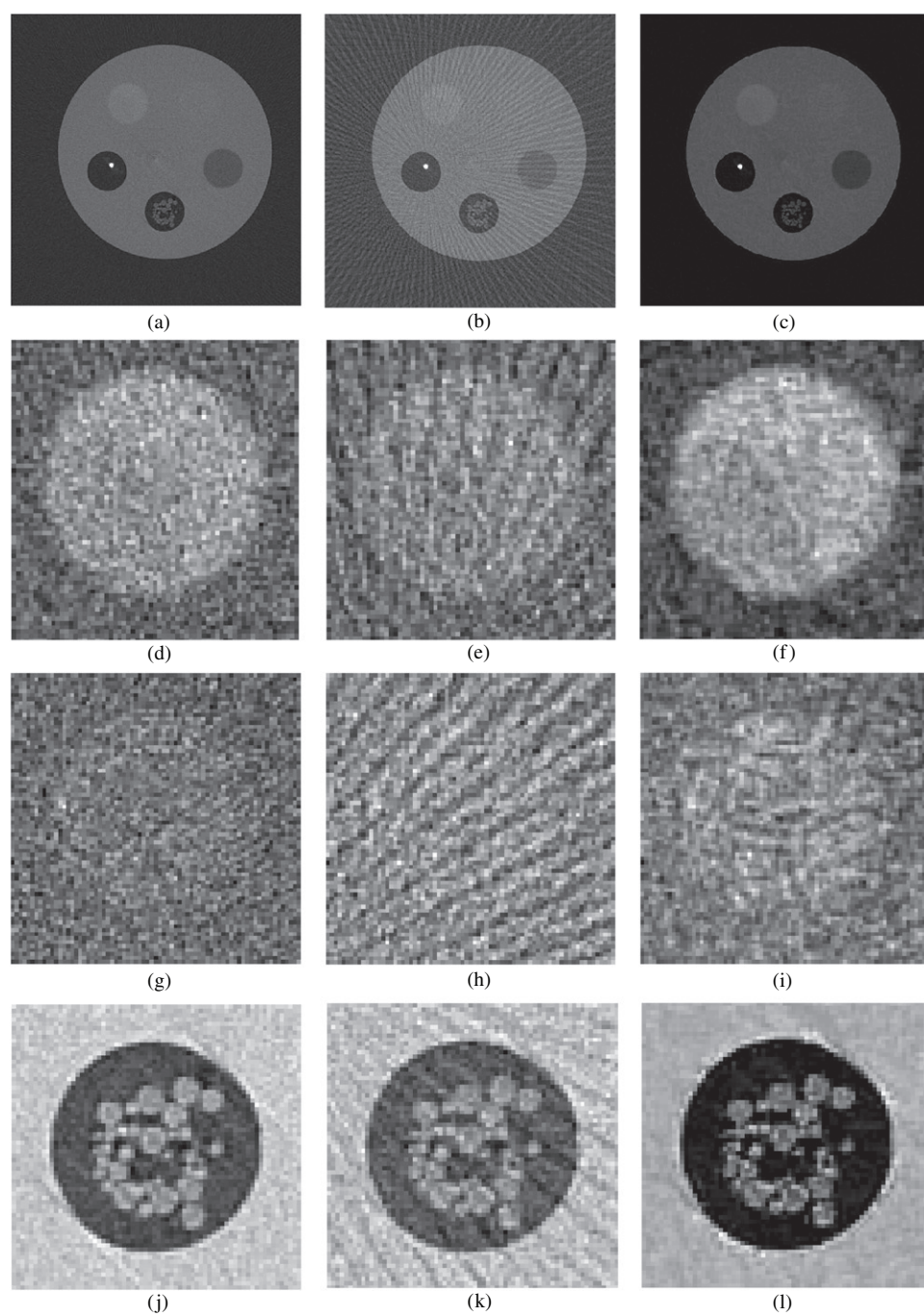


**Figure 4.** Experimental results for the x-ray absorption CT modality. From left to right: the columns represent FBP with 200-projections, FBP with 80-projections and EST-NL with 80-projections. From top to bottom: comparison of the full field of view, medium contrast insert, low-contrast insert and resolution insert. The displayed FOV in the first row is 362 by 362 pixels.



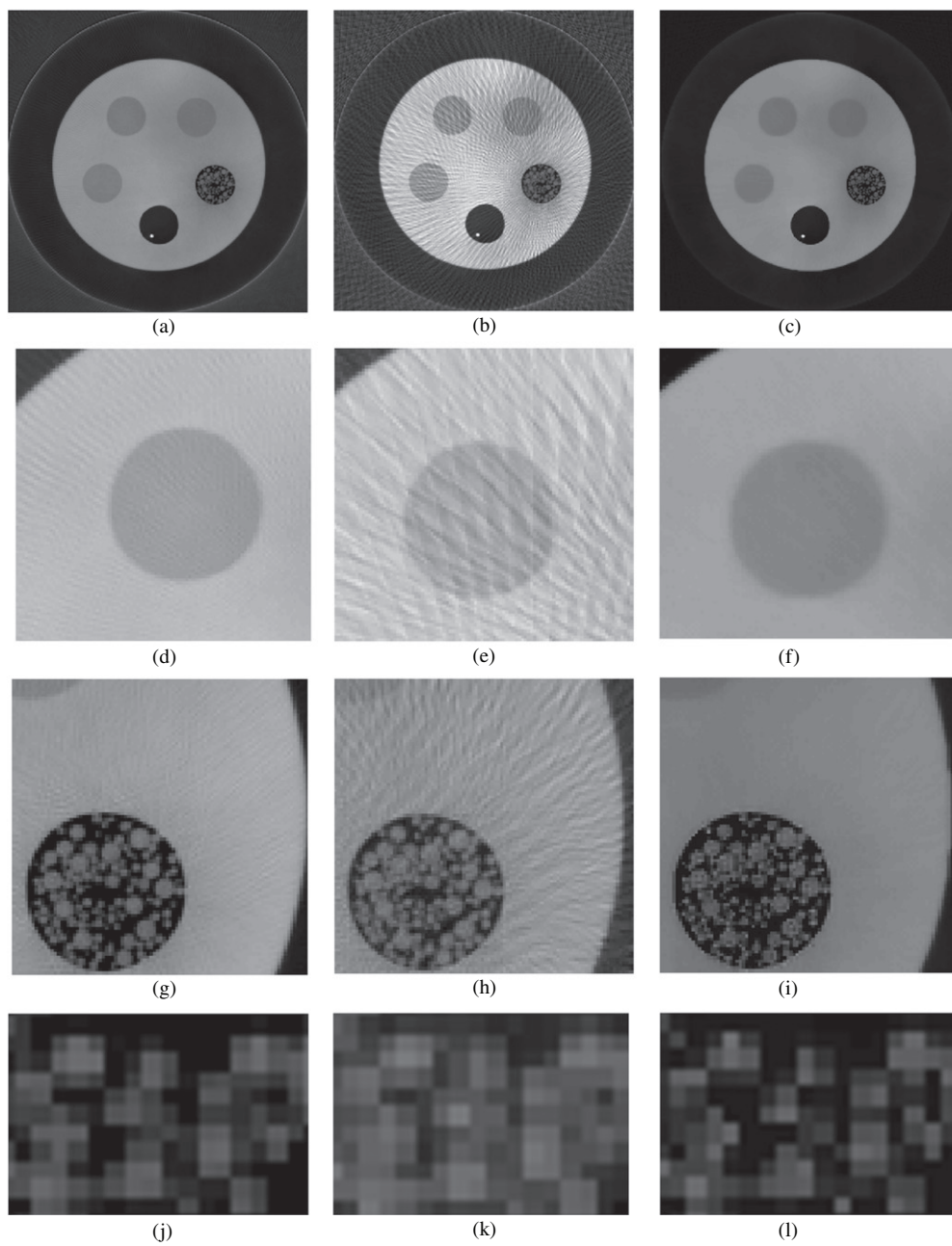


**Figure 5.** Experimental results for the x-ray phase contrast CT modality. From left to right: the columns represent FBP with 200-projections, FBP with 60-projections and EST-NL with 60-projections. From top to bottom: comparison of the full field of view, contrast insert, resolution insert and zoomed area of resolution insert. The displayed FOV in the first row is  $384 \times 384$  pixels.

is smoother than that of both the 60- and 200-projection FBP reconstruction. The resolution is visually assessed in the third and fourth row. The 60-projection FBP has visibly noticeable lower resolution as determined by the separation of the beads when compared to the 200-projection FBP, while the 60 EST-NL reconstruction presents with comparable separation of fine features to the 200-projection FBP.

## 5. Conclusion

Tomographic reconstruction from a limited number of projections provides a method to simultaneously reducing the radiation dose, and in many cases the acquisition time. We have developed a method of tomographic acquisition and regularized iterative Fourier-based reconstruction, termed equally sloped tomography (EST), which through the use of mathematical and physical constraints provides a methodology for tomographic reconstruction using only a fraction of the number of projections as conventionally required in tomographic application. Simulation and experimental results in both the x-ray absorption and phase contrast CT modalities have indicated feasibility of reducing the number of projections by a factor of 60–75% while still achieving equal or better image quality relative to conventional reconstructions. The combination of the developed methodology and synchrotron x-ray sources hence allows for low-dose x-ray absorption and phase-contrast CT applications in biology and medicine. Finally, as methodology pertains to general tomographic reconstruction, it can also be applied to medical x-ray CT scanners for low-dose image reconstructions, which will be presented in subsequent papers.

## Acknowledgments

We thank Professors M F McNitt-Gray, J J DeMarco, S J Osher, A F Chatziioannou, O Levi and Dr E K Lee for stimulating discussions. This work was partially supported by UC Discovery/TomoSoft Technologies grant IT107-10166, and National Institutes of Health grant GM081409-01A1.

## References

- Abbey B, Nugent K A, Williams G J, Clark J N, Peele A G, Pfeifer M A, de Jonge M and McNulty I 2008 Keyhole coherent diffractive imaging *Nat. Phys.* **4** 394–8
- Averbuch A, Coifman R R, Donoho D L, Israeli M and Shkolnisky Y 2008a A framework for discrete integral transformations I—the pseudopolar Fourier transform *SIAM J. Sci. Comput.* **30** 785–803
- Averbuch A, Coifman R R, Donoho D L, Israeli M, Shkolnisky Y and Sedelnikov I 2008b A framework for discrete integral transformations II—the 2D discrete radon transform *SIAM J. Sci. Comput.* **30** 785–803
- Bailey D H and Swartztrauber P N 1991 The fractional Fourier transform and applications *SIAM Rev.* **33** 389–404
- Bech M, Bunk O, David C, Ruth R, Rifkin J, Loewen R, Feidenhans'l R and Pfeiffer F 2009 Hard x-ray phase-contrast imaging with the Compact Light Source based on inverse Compton x-rays *J. Synchrotron Radiat.* **16** 43–7
- Briggs W L and Henson V E 1995 *The DFT: An Owner's Manual for the Discrete Fourier Transform* (Philadelphia, PA: SIAM)
- Buades A, Coll B and Morel J M 2005 A review of image denoising algorithms, with a new one *Multiscale Model. Simul.* **4** 490–530
- Buades A, Coll B and Morel J M 2006 Image enhancement by non-local reverse heat equation *Technical Report 22* CMLA
- Bushberg J T 2002 *The Essential Physics of Medical Imaging* (Philadelphia, PA: Williams & Wilkins)
- Candès E, Romberg J and Tao T 2006 Exact signal reconstruction from highly incomplete frequency information *IEEE Trans. Inf. Theory* **52** 489–509
- Cloetens P, Ludwig W, Baruchel J, Guigay J-P, Pernot-Rejmánková P, Salomé-Pateyron M, Schlenker M, Buffière J-Y, Maire E and Peix G 1999 Hard x-ray phase imaging using simple propagation of a coherent synchrotron radiation beam *J. Phys. D: Appl. Phys.* **32** A145–51

- Comtat C, Kinahan P E, Defrise M, Michel C and Townsend D W 1998 Fast reconstruction of 3D PET data with accurate statistical modeling *IEEE Trans. Nucl. Sci.* **45** 1083–9
- Connor D M, Hallen H D, Lalush D S, Sumner D R and Zhong Z 2009 Comparison of diffraction-enhanced computed tomography and monochromatic synchrotron radiation computed tomography of human trabecular bone *Phys. Med. Biol.* **54** 6123–33
- De Francesco S and Ferreira da Silva A M 2004 Efficient NUFFT-based direct Fourier algorithm for fan beam CT reconstruction *Proc. SPIE* **5370** 666–77
- Delaney A H and Bresler Y 1996 A fast and accurate Fourier algorithm for iterative parallel-beam tomography *IEEE Trans. Image Process.* **5** 740–53
- Edholm P R and Herman G T 1987 Linograms in image reconstruction from projections *IEEE Trans. Med. Imaging* **6** 301–7
- Edholm P R, Herman G T and Roberts D A 1988 Image reconstruction from linograms: implementation and evaluation *IEEE Trans. Med. Imaging* **7** 239–46
- Frank J 2006 *Electron Tomography: Methods for Three-Dimensional Visualization of Structures in the Cell* 2nd edn (Berlin: Springer)
- Fritsch F N and Carlson R E 1980 Monotone piecewise cubic interpolation *SIAM J. Numer. Anal.* **17** 238–46
- Gayou O and Miften M 2007 Commissioning and clinical implementation of a mega-voltage cone beam CT system for treatment localization *Med. Phys.* **34** 3183–92
- Gilboa G and Osher S 2008 Nonlocal operators with applications to image processing *Multiscale Model. Simul.* **7** 1005–28
- Greengard L and Lee J-Y 2004 Accelerating the nonuniform fast Fourier transform *SIAM Rev.* **46** 443–54
- ICRU 1989 Tissue substitutes in radiation dosimetry and measurement *ICRU Report No 44* (Bethesda, MD: ICRU)
- Jiang H, Song C, Chen C-C, Xu R, Raines K S, Fahimian B P, Lu C-H, Lee T K, Nakashima A, Urano J, Ishikawa T, Tamanoi F and Miao J 2010 Quantitative 3D imaging of whole, unstained cells by using x-ray diffraction microscopy *Proc. Natl. Acad. Sci. USA* **107** 11234–9
- Kak A C and Slaney M 2001 *Principles of Computerized Tomographic Imaging* (Philadelphia, PA: SIAM)
- Labiche J, Maton O, Pascarelli S, Newton M A, Ferre G C, Curfs C, Vaughan G, Homs A and Carreiras D F 2007 The FReLoN camera as a versatile x-ray detector for time resolved dispersive EXAFS and diffraction studies of dynamic problems in materials science, chemistry, and catalysis *Rev. Sci. Instrum.* **78** 091301
- Langer M, Cloetens P, Guigay J P and Peyrin F 2008 Quantitative comparison of direct phase retrieval algorithms in in-line phase tomography *Med. Phys.* **35** 4556–66
- Lawton W 1988 A new polar Fourier transform for computer-aided tomography and spotlight synthetic aperture radar *IEEE Trans. Acoust. Speech Signal Process.* **36** 931–3
- Lee E, Fahimian B P, Iancu C V, Suloway C, Murphy G E, Wright E R, Castano-Diez D, Jensen G J and Miao J 2008 Radiation dose reduction and image enhancement in biological imaging through equally sloped tomography *J. Struct. Biol.* **164** 221–7
- Lewis R A 2004 Medical phase contrast x-ray imaging: current status and future prospects *Phys. Med. Biol.* **49** 3573–83
- Mao Y, Fahimian B P, Osher S and Miao J 2010 Development and optimization of tomographic reconstruction algorithms utilizing equally sloped tomography *IEEE Trans. Image Process.* **19** 1259–68
- Matej S, Fessler J A and Kazantsev I G 2004 Iterative tomographic image reconstruction using Fourier-based forward and back-projectors *IEEE Trans. Med. Imaging* **23** 401–12
- Mersereau R M and Oppenheim A V 1974 Digital reconstruction of multidimensional signals from their projections *Proc. IEEE* **62** 1319–38
- Miao J, Charalambous P, Kirz J and Sayre D 1999 Extending the methodology of x-ray crystallography to allow imaging of micrometre-sized non-crystalline specimens *Nature* **400** 342–4
- Miao J, Chen C-C, Song C, Nishino Y, Kohmura Y, Ishikawa T, Ramunno-Johnson D, Lee T-K and Risbud S H 2006 Three-dimensional GaN-Ga<sub>2</sub>O<sub>3</sub> core shell structure revealed by x-ray diffraction microscopy *Phys. Rev. Lett.* **97** 215503
- Miao J, Förster F and Levi O 2005 Equally sloped tomography with oversampling reconstruction *Phys. Rev. B* **72** 052103
- Miao J, Sayre D and Chapman H N 1998 Phase retrieval from the magnitude of the Fourier transform of non-periodic objects *J. Opt. Soc. Am. A* **15** 1662–9
- Momose A, Takeda T, Itai Y and Hirano K 1996 Phase-contrast x-ray computed tomography for observing biological soft tissues *Nat. Med.* **2** 473–5
- Natterer F 2001 *The Mathematics of Computerized Tomography* (Philadelphia, PA: SIAM)
- Nickoloff E L 1988 Measurement of the PSF for a CT scanner: appropriate wire diameter and pixel size *Phys. Med. Biol.* **33** 149–55

- Nickoloff E L and Riley R 1985 A simplified approach for modulation transfer function determinations in computed tomography *Med. Phys.* **12** 437–42
- Nugent K A, Gureyev T E, Cookson D F, Paganin D and Barnea Z 1996 Quantitative phase imaging using hard x-rays *Phys. Rev. Lett.* **77** 2961
- Pfeifer M A, Williams G J, Vartanyants I A, Harder R and Robinson I K 2006 Three-dimensional mapping of a deformation field inside a nanocrystal *Nature* **442** 63–6
- Raines K S, Salha S, Sandberg R L, Jiang H, Rodriguez J A, Fahimian B P, Kapteyn H C, Du J and Miao J 2010 Three-dimensional structure determination from a single view *Nature* **463** 214–7
- Rudin L I, Osher S and Fatemi E 1992 Nonlinear total variation based noise removal algorithms *Physica D* **259**–68
- van Heel M and Schatz M 2005 Fourier shell correlation threshold criteria *J. Struc. Bio.* **151** 250–62
- Ware A F 1998 Fast approximate Fourier transforms for irregularly spaced data *SIAM Rev.* **40** 838–56
- Weitkamp T, David C, Bunk O, Bruder J, Cloetens P and Pfeiffer F 2008 X-ray phase radiography and tomography of soft tissue using grating interferometry *Eur. J. Radiol.* **68** S13–7
- Zhang-O'Connor Y and Fessler J A 2006 Fourier-based forward and back-projectors in iterative fan-beam tomographic image reconstruction *IEEE Trans. Med. Imaging* **25** 582–9
- Zubal I G, Harrell C R, Smith E O, Rattner Z, Gindi G and Hoffer P B 1994 Computerized three-dimensional segmented human anatomy *Med. Phys.* **21** 299–302